Numerical simulation of bubble deformation
and breakup under simple linear shear flows

Mitsuhiro Ohta*
Department of Mechanical Science, Graduate School of Technology,
Industrial and Social Sciences, Tokushima University,
2-1 Minamijyousanjima-cho,Tokushima 770-8506, Japan

Tetsuya Ueta
Department of Mechanical Engineering, Graduate School of Advanced Technology and Science,
Tokushima University, 2-1 Minamijyousanjima-cho,Tokushima 770-8506, Japan

Yozo Toei
High Performance Plastics Company, Sekisui Chemical Co., Ltd.,
2-1 Hyakuyama, Mishimagun Shimamoto-cho, Osaka 618-0021, Japan

Edwin Jimenez
Department of Computing and Mathematical Sciences,
MC 305-16 California Institute of Technology, Pasadena, CA 91125, USA

Mark Sussman
Department of Mathematics, Florida State University, Tallahassee, FL 32306, USA
(Dated: April 3, 2024)

Numerical simulations for the deformation and breakup of a bubble in liquids undergoing simple linear shear flow are presented. Numerical results are obtained using a hydrodynamic scheme with formal second-order accuracy based on a coupled level set/volume-of-fluid (CLSVOF) method. To verify our numerical algorithm, and to provide a basis for comparison, we also present simulation results which compare with previous, more popular, simulations of drop deformation and rupture. The numerical results reveal that the shear-induced bubble deformation and breakup process differs significantly from that of the analogous drop system under similar flow conditions. The first distinguishing factor for bubble breakup is that the magnitude of shear flow necessary for rupture is much larger than that in the drop system case. In other words, a larger Reynolds number is necessary to induce bubble breakup. The second distinct feature of the bubble system versus the drop system is that the bubble does not maintain a stable deformed shape as the parameters of the system approach the critical "breakup" Reynolds number. It is asserted that the differences in morphology for a bubble undergoing breakup, versus a drop in the same process, can be attributed to the density and viscosity ratio of the corresponding two-phase flow systems. The critical conditions for bubble breakup with respect to the Reynolds and capillary numbers are determined for several cases.

Keywords: Bubble deformation, bubble breakup, shear flow, CFD

I. INTRODUCTION

The study of the deformation *and breakup* of a drop in immiscible viscous liquids undergoing simple linear shear flow has been investigated extensively due to its fundamental importance in connection with emulsion and materials processing, mixing and reaction devices. The pioneering experimental work of this problem was performed by Taylor in the early 1930s [1, 2], and the subsequent theoretical and experimental progress up to the 1980s and 1990s was reviewed in [3] and [4], respectively. By the 2000s, progress in computational fluid dynamics (CFD) techniques and increased access to powerful computing resources led to a surge of research focused on direct simulations of this problem. In particular, detailed computational investigations of drop breakup, based on a Volume-of-Fluid (VOF) method [5] were presented in [6–13]. Since then, the literature on computational studies on the deformation and breakup of a single or several drops in shear flow has continued to grow [14–25] and a variety of numerical techniques have been developed to tackle this problem, including boundary-integral approaches [26, 27], lattice Boltzmann methods

* Also in the Department of Mechanical Engineering, Graduate School of Advanced Technology and Science, Tokushima University; m-ohta@tokushima-u.ac.jp

[20, 28], front tracking schemes [29], and interface-capturing level set methods [30]. In contrast, few computational studies on bubble deformation *and breakup* can be found. We remark that there has been a number of articles on the study of lift of *slightly* deformable bubbles[31, 32]. We reiterate though, that for bubble deformation *and breakup* in shear flows, only a few articles exist: [33, 34]. In these previous studies, the dynamics (e.g. rotation angle) of bubble deformation in shear flow was mainly examined. Concerning bubble breakup, Wei et al. [33] presented only one numerical result for a bubble breakup process under the condition of Ca (Capillary number) $= 35$. Bubble dynamics in shear flow, *including breakup*, is of critical importance for a variety of scientific and engineering processes. We refer the reader to the following experimental studies relating to bubble deformation in foaming processes, microfluidic devices, and micro bubbles in the blood circulation system,[35–38]. In particular, it is the study of bubble deformation as it pertains to high performance plastics applications which motivates this work. In this article, we present computational studies of shear-driven deformation *and breakup* of a bubble in insoluble viscous liquids. Studying bubble break-up via computation rather than experiments simplifies the process of setting a combination of precise simple shear flow conditions, low Ca conditions, low density ratio, and low viscosity ratios. The physical properties that distinguish bubble and drop studies are expressed in terms of the density ratio $\lambda = \rho_{\rm b}/\rho_{\rm m}$ and the viscosity ratio $\eta = \mu_{\rm b}/\mu_{\rm m}$, where ρ is the fluid density, μ is the viscosity and the subscripts "b" and "m" denote the "bubble" or "drop" and the "matrix fluid", respectively. For a bubble in an insoluble viscous liquid, $\lambda \simeq 0$ and $\eta \simeq 0$, whereas most studies dealing with a drop in an immiscible viscous liquid take $\lambda = 1$ and $\eta \simeq 1$.

In this work we focus on identifying critical flow states numerically, in terms of dimensionless quantities, that specify the extreme conditions at which a bubble or drop in shear flow first transitions from deformation to breakup. We validate our numerical method through comparisons with previous shear-driven drop dynamics results and we also examine the effect of drop deformation and breakup sensitivity on domain and grid size. An advantage of studying shear-driven bubble deformation and breakup computationally, rather than experimentally, is that we can easily modify fluid physical properties to ascertain the sensitivity of deformation and breakup to physical parameters. In our computations, the time-evolution of the boundary between gas and liquid is tracked with a coupled level set/volume-of-fluid (CLSVOF) interface capturing algorithm [39, 40]. We focus on determining critical physical conditions in which the breakup of a bubble occurs in shear flow because it is important to identify the parameter regimes in which a relatively simple system transitions from stable to unstable. Specifically, we identify the critical Reynolds number ($Re_{\rm c}$) corresponding to the bubble breakup onset condition as a function of Ca. The critical Reynolds number, $Re_{\rm c}$, for drop breakup was reported previously by [6]. In previous studies on the motion of bubble deformation in a simple shear flow [36, 41], only findings for bubble deformation under very low Re number conditions ($Re \ll 1$) have been reported. In this work we determine, for the first time, the critical Reynolds number ($Re \gg 1$) that leads to *bubble* breakup. Additionally, our computational studies reveal characteristics that distinguish the deformation and breakup processes of a drop versus those of a bubble.

II. PROBLEM DESCRIPTION

Figure 1(a) shows a schematic of the computational system for our studies of a bubble (or drop) in shear flow. The computational domain consists of a three-dimensional rectangular domain of L (length) $\times W$ (width) $\times H$ (height). The size of L, W and H was determined after consideration of numerical result sensitivity to domain size; numerical studies of domain-size dependence are presented in Section III C. All computational results that follow were obtained from numerical solutions of the three-dimensional governing equations for gas-liquid/liquid-liquid flows. Computations are initialized with a spherical bubble (or drop) of radius $R = 5$ mm set at the center of the computational domain. The bubble (or drop) is then subjected to a linear shear flow generated by the motion of the top and bottom plates, which have constant velocity $+V$ and $-V$, respectively. In the interior of the domain, the initial velocity condition is assumed to be a simple linear profile and periodic boundary conditions are imposed along the x and y directions.

Mathematically, the initial and boundary conditions are described as follows:

$$\phi(x,y,z,0) = \sqrt{(x - \frac{L}{2})^2 + (y - \frac{W}{2})^2 + (z - \frac{H}{2})^2} - R \tag{1}$$

$$\mathbf{u}(x,y,z,0) = \begin{pmatrix} \frac{2V}{H}(z - \frac{H}{2}) \\ 0 \\ 0 \end{pmatrix}$$

$$\phi(x+L,y,z,t) = \phi(x,y,z,t) \qquad \phi(x,y+W,z,t) = \phi(x,y,z,t)$$

$$\mathbf{u}(x,y,H,t) = \begin{pmatrix} V \\ 0 \\ 0 \end{pmatrix} \qquad \mathbf{u}(x,y,0,t) = \begin{pmatrix} -V \\ 0 \\ 0 \end{pmatrix}$$

$$\mathbf{u}(x+L,y,z,t) = \mathbf{u}(x,y,z,t) \qquad \mathbf{u}(x,y+W,z,t) = \mathbf{u}(x,y,z,t)$$

$\phi(x,y,z,t)$ is a material indicator function which is positive in the "matrix" fluid and negative in the bubble (or drop) fluid. $\mathbf{u}(x,y,z,t)$ is the velocity.

Common dimensionless physical parameters used to describe gas-liquid or liquid-liquid two-phase flows include the Reynolds (Re), Weber (We) (or Ca ($= We/Re$)) and Froude (Fr) numbers. Gas-Liquid and Liquid-Liquid two-phase flow problems are also determined by the density ratio λ and the viscosity ratio η. In the present study, the effect of gravity is not considered so that we ignore the effect of the Fr number.

When comparing with previous drop studies, we fix $\lambda = 1$. As a result, (for $\lambda = 1$) the following dimensionless physical parameters are used to describe the problem of drop deformation/breakup in shear flow

$$Re = \frac{\rho_m U R}{\mu_m}, \quad Ca = \frac{\mu_m U}{\sigma}, \quad \eta = \frac{\mu_b}{\mu_m} \qquad m = \text{matrix fluid} \tag{2}$$

U is the velocity scale and σ denotes the surface tension. For the problem of shear-induced drop deformation and breakup, the velocity is set to $U = \Gamma R$, where the shear-rate is $\Gamma = 2V/H$. As mentioned in the introduction, most previous drop studies set $\eta = 1$ (e.g. [6]). Thus, for comparison with previous drop deformation and breakup problems, we set $\lambda = \eta = 1$ (and also neglect the effect of gravity so that $g = 0$). On the other hand, in our computations for bubble deformation, we set the density and viscosity of air to be $\rho_b = 1.2$ kg/m^3 and $\mu_b = 1.8 \times 10^{-5}$ Pa·s respectively. We emphasize that for consistency with previous studies ([6, 20, 24, 36, 41]), we computationally examine the deformation and breakup of a bubble in simple linear shear flow as a function of the Re and Ca numbers. That is to say, by setting $g = 0$, we are isolating the effect of only varying Re and Ca on bubble deformation and breakup. In our controlled study, we determine the critical Re_c versus Ca curve in which Re_c corresponds to the threshold of bubble (or drop) breakup. We determine the critical Re_c versus Ca curve for strategic pairs of the density ratio and viscosity ratio.

In our computations, the density of the matrix fluid is fixed at $\rho_m = 1000$ kg/m^3. The surface tension at the bubble (drop) interface is $\sigma = 2.5 \times 10^{-2}$ N/m. The values of Re and Ca in our simulations are controlled by changing the values of μ_m and V. For studying bubble deformation and break-up, the density and viscosity ratios satisfy $\lambda = 1.2 \times 10^{-3}$ and $\eta < 1.0 \times 10^{-3}$.

III.   NUMERICAL ANALYSIS

A.   Numerical method and governing equations

Numerical results were obtained using the interface capturing Coupled Level Set and Volume of Fluid (CLSVOF) method [39, 40], which is based on a fixed grid finite volume algorithm. The CLSVOF method is a robust numerical technique that combines some of the advantages of the Volume of Fluid (VOF) method ([5]) and the Level Set (LS) ([30]) method while overcoming their weaknesses. In the VOF method, the Volume Fraction function, F, is used to represent the interface. The values of F correspond to the volume fraction of liquid in a given computational cell. In other words, $F = 0$ when a computational cell contains only gas and $F = 1$ when a computational cell contains only liquid. If $0 < F < 1$, then a computational cell contains the gas-liquid interface. The VOF method has a great advantage over the LS method in that accurate algorithms for advecting F can be applied so that mass/volume is conserved up to machine precision while still maintaining a sharp representation of the interface. On the other hand, the disadvantage of the VOF method in comparison to the LS method is that tangled and difficult reconstruction procedures are required for determining the slope of the piecewise linear VOF reconstructed interface. In the LS method, the signed distance function ϕ (LS function) is used to track the interface. The interface is implicitly
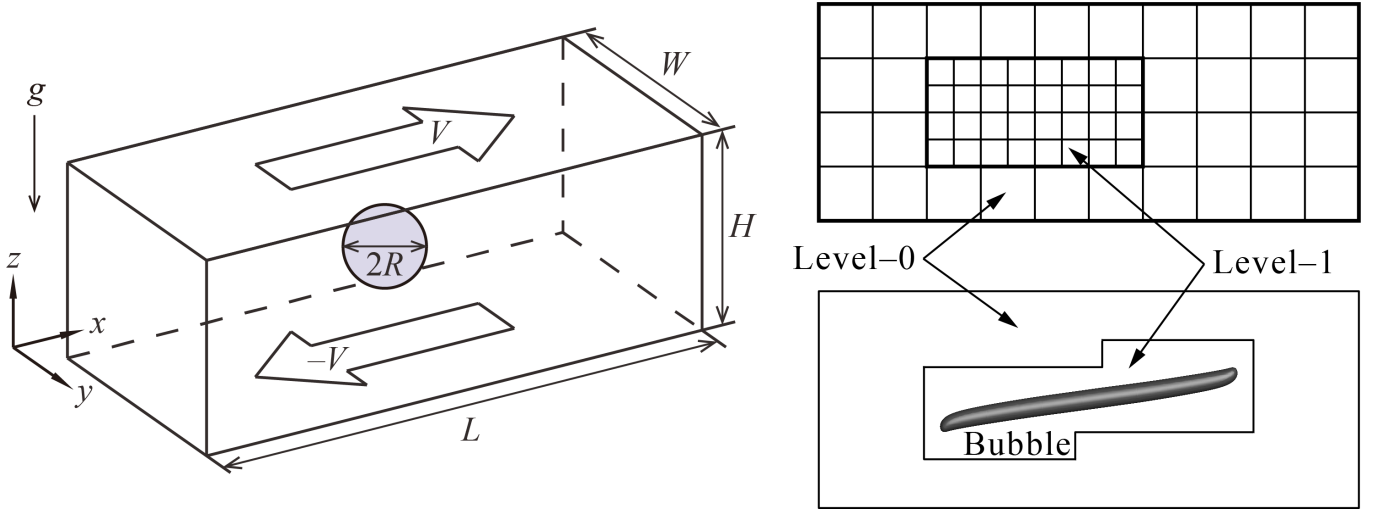
FIG. 1. (a) Computational domain schematic for a bubble or drop in shear flow. Gravity is set to zero in our computations in order to isolate the effects of density and viscosity ratios. (b) (*upper panel*) a two-level adaptive mesh refinement (AMR) grid schematic corresponding to one of our simulations; (*lower panel*) snapshot of bubble deformation in simple linear shear flow.

represented by the set of points in which $\phi = 0$. Liquid and gas regions are defined as $\phi > 0$ in the liquid and $\phi < 0$ in the gas, respectively. One of the advantages of the LS method is that one can track and represent smoothly the interface, but the LS method has the disadvantage that mass/volume is not explicitly conserved. In the CLSVOF method, the coupling between the LS function and the VOF function occurs when computing the normal of the reconstructed interface in the VOF calculation process and also when assigning the LS function with the exact signed normal distance to the reconstructed interface in the LS calculation process. That is to say, the piecewise linear approximation (the volume-of-fluid reconstruction step) for the VOF method is determined using the unit normal vector ($\boldsymbol{n}$) estimated from information of the LS function. By taking advantage of both methods, the evolution of the liquid-gas interface location can be computationally captured in such a way so that volume/mass is preserved to machine precision and at the same time, the interface normals and the surface tension force (which is proportional to the interface curvature) can be straightforwardly derived from the smooth level set function.

In our studies, the two-phase fluid flow is comprised of air and a viscous Newtonian liquid. The Heaviside function, $\mathcal{H}(\phi)$, which is defined as

$$\mathcal{H}(\phi) = \begin{cases} 1 & \phi \geq 0 \\ 0 & \phi < 0 \end{cases} \tag{3}$$

will be used below to distinguish each of the two fluids. A single set of three-dimensional equations governs the motion of both fluids, which are taken to be incompressible, and consists of the continuity equation and the Navier-Stokes equations with surface tension forces:

$$\nabla \cdot \mathbf{u} = 0 \tag{4}$$

$$\frac{\partial \mathbf{u}}{\partial t} + (\mathbf{u} \cdot \nabla)\mathbf{u} = \frac{1}{\rho}\nabla \cdot (-p\mathbf{I} + 2\mu\mathbf{D}) + \mathbf{g} - \frac{\sigma\kappa}{\rho}\nabla\mathcal{H} \tag{5}$$

where $\mathbf{u}$ is the velocity vector, t represents time, p is the pressure, $\mathbf{I}$ is the unit tensor, $\mathbf{D}$ is the rate of deformation tensor ($\mathbf{D} = \frac{1}{2}(\nabla\mathbf{u} + (\nabla\mathbf{u})^T)$), ρ is the density, μ is the viscosity, κ is the interfacial curvature, and the Heaviside function $\mathcal{H}(\phi)$ is a function of the level set (LS) function ϕ. The singular Heaviside gradient term in the right hand side of equation (5) is a body force representing the surface tension force and is equivalent to specifying that the jump in the normal stress is equal to $\sigma\kappa$ [42]. The surface tension force expressed by the singular Heaviside gradient term acts only on the gas-liquid interface. The sharp interface "Ghost Fluid Method" [43] is used to discretize the gradient of the Heaviside function as it appears in the surface tension force term. This force, upon discretization, is only non-zero across cells in which the level set function changes sign.

The interfacial curvature κ is computed with second order accuracy directly from the volume-of-fluid (VOF) function using the height function technique [40, 44]. We remark that we get the same results if we were to compute κ directly from the LS function using the "level set" height function technique.

Since ρ and μ are taken to be constant in each fluid, with a jump at the interface, they can be expressed in terms of the Heaviside function,

$$\rho = \rho_{\mathrm{m}}\mathcal{H} + \rho_{\mathrm{b}}(1 - \mathcal{H}), \qquad \mu = \mu_{\mathrm{m}}\mathcal{H} + \mu_{\mathrm{b}}(1 - \mathcal{H}). \tag{6}$$

The subscripts "b" and "m" refer to "drop or bubble" and "matrix fluid", respectively. To represent the free surface with the CLSVOF method, we must evolve the solution to both the VOF equation for F and the LS equation for ϕ:

$$\frac{\partial F}{\partial t} + (\mathbf{u} \cdot \nabla)F = 0, \qquad \frac{\partial \phi}{\partial t} + (\mathbf{u} \cdot \nabla)\phi = 0. \tag{7}$$

In all computations the discretized variables p, ϕ and F are located at cell centers and the discrete variable $\mathbf{u}$ is located at cell face centers. Our computations are performed using an overall second-order accurate hydrodynamic scheme. The spatial discretization uses second-order accurate, slope-limited, upwind techniques for the nonlinear advective terms. The velocity and pressure fields are computed using an implicit pressure projection procedure.

The temporal discretization of our numerical method is an operator split projection method as described by [40]. An outline of our method is as follows (see [40], section 4, for more details):

Timestep Δt: The timestep is governed by the CFL condition and surface tension (section 5.7 of [40]):

$$\Delta t < \min_{i,j,k}\left(\frac{\Delta x}{2|U^n|}, \frac{1}{2}\sqrt{\frac{\rho^L}{8\pi\sigma}}\Delta x^{3/2} \right)$$

Step 1. CLSVOF interface advection:

$$\phi^{n+1} = \phi^n - \Delta t[\mathbf{u} \cdot \nabla\phi]^n$$
$$F^{n+1} = F^n - \Delta t[\mathbf{u} \cdot \nabla F]^n$$

Step 2. Nonlinear advective force terms:

$$\mathcal{A} = [\mathbf{u} \cdot \nabla\mathbf{u}]^n$$

Step 3. Viscosity force:

$$\frac{\mathbf{u}^* - \mathbf{u}^n}{\Delta t} = -\mathcal{A} + g\vec{z} - [\nabla p/\rho]^n + \frac{1}{2}\frac{\nabla \cdot (2\mu\mathbf{D}^n) + \nabla \cdot (2\mu\mathbf{D}^*)}{\rho}$$

Step 4. Pressure projection and ghost fluid surface tension algorithm:

$$\mathbf{V} = \mathbf{u}^n + \Delta t(-\mathcal{A} + g\vec{z} + \frac{1}{2}\frac{\nabla \cdot (2\mu\mathbf{D}^n) + \nabla \cdot (2\mu\mathbf{D}^*)}{\rho})$$

$$\mathbf{V} = \mathbf{V} - \Delta t\frac{\sigma\kappa(\phi^{n+1})}{\rho}\nabla\mathcal{H}(\phi^{n+1})$$

$$\nabla \cdot \frac{\nabla p}{\rho} = \frac{1}{\Delta t}\nabla \cdot \mathbf{V}$$

$$\mathbf{u}^{n+1} = \mathbf{V} - \Delta t\frac{\nabla p}{\rho}$$

To make efficient use of computational resources, our numerical simulations utilize an adaptive hierarchy of grids based on a dynamic adaptive mesh refinement (AMR) technique [45]. Adaptive grids are dynamically adjusted based on the location of the deforming gas-liquid interface. In the AMR technique the grid resolution is increased in regions near the interface while a coarser grid is used where the flow is relatively steady. The upper panel of Figure 1(b) displays a schematic view of the hierarchical grid structure and the lower panel corresponds to an actual computational example for bubble deformation in simple linear shear flow. In general, the mesh hierarchy is composed of different levels of refinement ranging from coarsest $\ell = 0$ ("level-0") to finest $\ell = \ell_{\max}$ ("level-$\ell_{\max}$"). The refinement ratio of one grid size ($\Delta x = \Delta y = \Delta z$) to the next finer level is two so that $\Delta x^{\ell+1} = 0.5\Delta x^{\ell}$. All computations in this study used an AMR system with a maximum prescribed level $\ell_{\max} = 1$ (as illustrated in the upper panel of Figure 1(b)). In our adaptive mesh refinement algorithm, the velocity in coarse grid cells that neighbor fine grid cells is interpolated from the coarse grid using bilinear interpolation in order to initialize "ghost" fine cells. Thus, the bilinear interpolation procedure produces interpolated fine grid data as a linear combination of the coarse grid data.

B. Validation of the numerical method

Numerical studies reported in this section are presented in order to verify the accuracy of our computational method. First, we compare quantitatively against the steady-state drop deformation results reported by Li et al. [6]. The shape of a deformed drop in simple linear shear flow is described in terms of the Taylor deformation parameter $D=(a-b)/(a+b)$, where a and b are the major and minor axes of the deformed drop. For consistency, we perform numerical simulations using CLSVOF over the same computational domain and grid size used in [6], which has dimensions $L(8R) \times W(4R) \times H(8R)$ (recall that R is the bubble/drop radius) and a level-0 grid size $\Delta x = \Delta y = \Delta z = R/8$; our two-level AMR grid structure also uses a finer level-1 grid size $\Delta x^{\ell=1} = \Delta y^{\ell=1} = \Delta z^{\ell=1} = R/16$. Numerical results are listed in Table I for D as a function of Re, with $Ca = 0.3$ and $\lambda = \eta = 1$ fixed in every case, obtained with the VOF method used in [6], and also with our CLSVOF algorithm. Table I indicates that our numerical results are in good agreement with previous computations for drop deformation and breakup.

TABLE I. Comparison of the Taylor deformation parameter D for a drop as a function of Re ($Ca = 0.3$, $\lambda = \eta = 1$). In all cases, the domain size is $L(8R) \times W(4R) \times H(8R)$, where R is the drop radius. CLSVOF method computations used a two-level AMR computational domain with a level-0 discretization $\Delta x^{\ell=0} = \Delta y^{\ell=0} = \Delta z^{\ell=0} = R/8$ and a level-1 discretization $\Delta x^{\ell=1} = \Delta y^{\ell=1} = \Delta z^{\ell=1} = R/16$.

Reynolds number	0.1	0.5	0.6	0.75
D(Li et al. ([6]))	0.3968	0.45	0.4768	Breakup
D(Our study)	0.3960	0.4570	0.4758	Breakup

Next, we examine the validation of our computational method in which we compare with the "bubble deformation in simple linear shear flow" results reported by Muller-Fischer et al. [36]. Muller-Fischer et al. [36] experimentally inquired into the bubble deformation under the condition of $Re \approx 0$. In our study, we computed the bubble deformation on a computational domain with dimensions $L(12R) \times W(6R) \times H(6R)$ and a computational grid in which the finest level grid size was $\Delta x^{\ell=1} = \Delta y^{\ell=1} = \Delta z^{\ell=1} = R/16$. Computations were performed for the conditions of $Ca = 0.96$ and $Ca = 1.63$ with $Re \approx 0$ ($Re = 5.0 \times 10^{-4}$), $\lambda = 1.2 \times 10^{-3}$ and $\eta \leq 1.2 \times 10^{-6}$. The parameters that we have prescribed are consistent with the experimental conditions by Muller-Fischer et al. [36]. Comparisons of our numerical results and previous experimental results ([36]) are tabulated in Table II. Additionally, in Table II, we also list experimental results with the condition of $Re \approx 0$ and $\lambda \approx \eta \approx 0$ by Rust and Manga ([41]). These experimental values by Rust and Manga ([41]) were obtained from the graph showing the relation of D vs Re ([41]). As is clear from Table II, our numerical results predicted larger values of D than experimental ones reported by Muller-Fischer et al. [36]. Nevertheless, we found that our numerical results are very close to the experimental results by Rust and Manga ([41]), which emphasizes the intrinsic difficulties associated with experimental investigations of bubble dynamics, even in simple linear shear flow. These comparisons suggest that our computational method is effective and robust at reproducing bubble dynamics in simple linear shear flow.

Finally, we present a comparison with numerical results for drop breakup reported in [8]. Figure 2 demonstrates drop breakup with pinch-off behavior for three Re and Ca conditions and with constant values of $\lambda = \eta = 1$ for all cases. The three cases that we consider correspond to (a) $Re = 10$, $Ca = 0.16$, (b) $Re = 12$, $Ca = 0.1753$, and (c) $Re = 15$, $Ca = 0.196$, and which are illustrated in Figures 2(a)-(c), respectively. The results reported in [8], which were obtained with a VOF method, are shown inside boxes while results obtained with our CLSVOF approach are displayed outside boxes. In the computations presented in [8], the dimensions $W = 4R$ and $H = 8R$ were fixed, while

TABLE II. Comparison of D for a bubble as a function of Ca ($Re \approx 0$, $\lambda \approx \eta \approx 0$). In all cases, the domain size is $L(12R) \times W(6R) \times H(6R)$. CLSVOF computations used a two-level AMR computational domain with a level-0 discretization $\Delta x^{\ell=0} = \Delta y^{\ell=0} = \Delta z^{\ell=0} = R/8$ and a level-1 discretization $\Delta x^{\ell=1} = \Delta y^{\ell=1} = \Delta z^{\ell=1} = R/16$.

Capillary number	0.96	1.63
D(Muller-Fischer et al. ([36]))	0.37	0.58
D(Rust and Manga ([41]))	0.71 ± 0.05	0.81 ± 0.02
D(Our study $\Delta x^{\ell=1} = R/16$)	0.63	0.75

(a) $Re = 10$, $Ca = 0.16$

(b) $Re = 12$, $Ca = 0.1753$

(c) $Re = 15$, $Ca = 0.196$
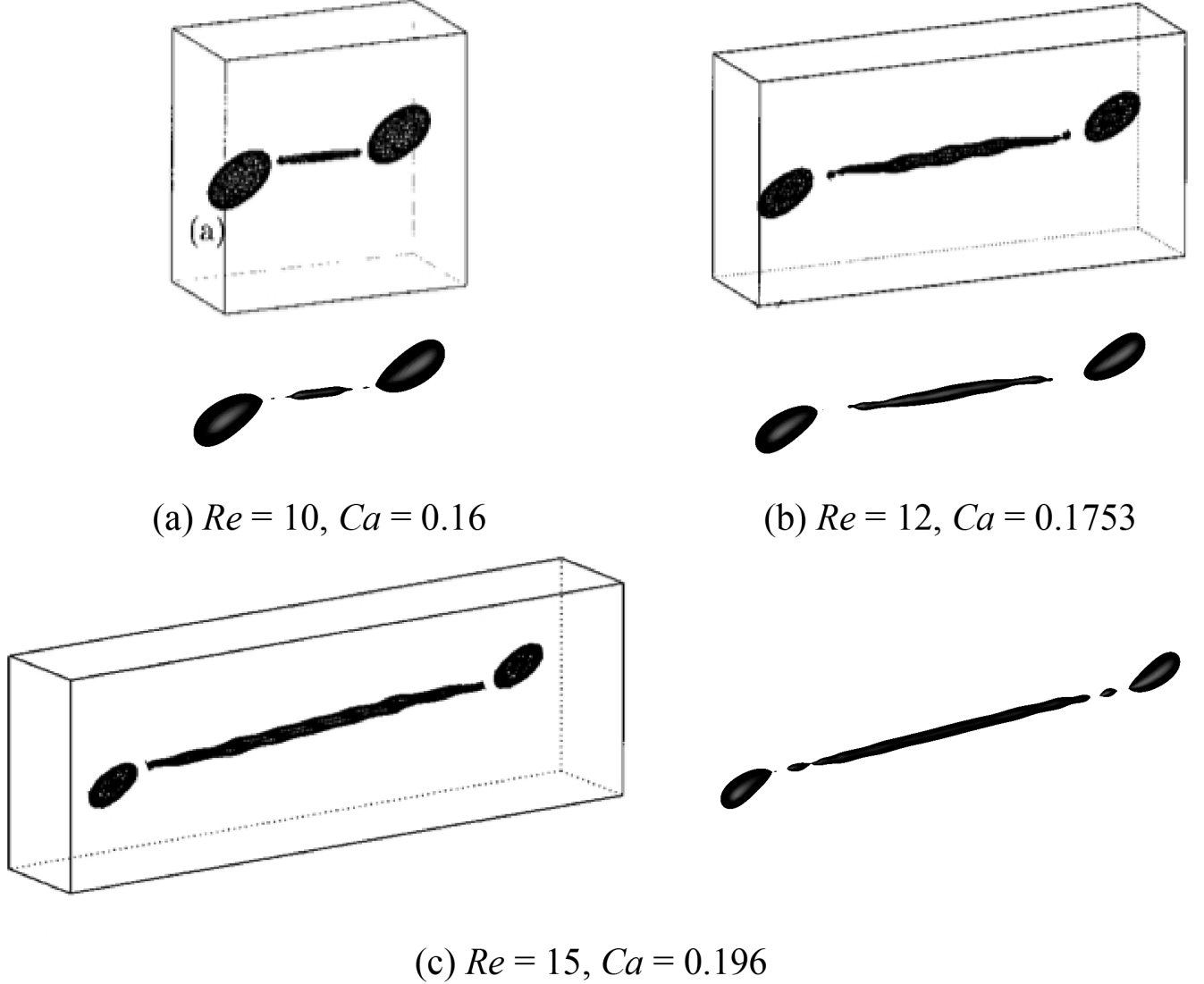
FIG. 2. Comparison with results reported in [8] (shown in boxes) for drop breakup in shear flow. In [8], the computational domain dimensions were $W = 4R$, $H = 8R$, and L was varied depending on the Re and Ca conditions. The grid size in [8] was set to $\Delta x = \Delta y = \Delta z = R/8$. Reprinted with permission from reference [8]. Copyright 2001, AIP Publishing. Results obtained with our CLSVOF algorithm, corresponding to each case in reference [8], are shown outside boxes. The CLSVOF method used a two-level AMR computational domain with a level-0 discretization $\Delta x^{\ell=0} = \Delta y^{\ell=0} = \Delta z^{\ell=0} = R/8$ and a level-1 discretization $\Delta x^{\ell=1} = \Delta y^{\ell=1} = \Delta z^{\ell=1} = R/16$. The onset of drop breakup is demonstrated for (a) $Re = 10$, $Ca = 0.16$, (b) $Re = 12$, $Ca = 0.1753$, and (c) $Re = 15$, $Ca = 0.196$. For all three Re and Ca conditions, $\lambda = \eta = 1$.

L was changed depending on Re and Ca conditions, and the grid size was set to $\Delta x = \Delta y = \Delta z = R/8$. To compare with their results, we performed simulations with the CLSVOF method over a two-level AMR computational domain

of the same dimensions and the same level-0 discretization: $\Delta x^{\ell=0} = \Delta y^{\ell=0} = \Delta z^{\ell=0} = R/8$; we set the finer level-1 grid size $\Delta x^{\ell=1} = \Delta y^{\ell=1} = \Delta z^{\ell=1} = R/16$. The results shown in Figure 2 verify that our numerical approach can reproduce the same drop breakup behavior presented in [8]. Slight differences between the results can be attributed to the increased resolution used in our study in the level-1 grid around the elongated drop.

The numerical validation studies performed in this section and the following section demonstrate that our numerical method can reliably determine the transition regions at which shear-induced bubble or drop deformation leads to breakup. We remark that in the next section, we demonstrate that we can expect an error of 3% for predicting the transition to break-up. The analysis in this section and the following also demonstrate that the error is reduced by a factor of 2 each time the grid is refined by a factor of 2. Also, we refer the reader to [46] in which we apply our CLSVOF method for bubble formation problems.

C. Consideration of domain and grid sizes

1. Selecting the appropriate domain size

The computational domain size used in numerical studies can affect the behavior of drop deformation and breakup. Referring to Figure 1(a), with an appropriately large domain length L and a fixed width $W = 4R$, the effect of the height H on drop behavior was examined in [6] for Stokes flows and various Ca conditions and in [20] for $Re = 1$ and $Ca = 0.27$. Other related studies investigated drop breakup sensitivity [7] and drop deformation sensitivity [9] with respect to the entire domain size.

TABLE III. Comparison of the Taylor deformation parameter D for a drop as a function of domain size ($Re = 0.75$, $Ca = 0.3$, $\lambda = \eta = 1$). CLSVOF method computations used a two-level AMR computational domain with a level-0 discretization $\Delta x^{\ell=0} = \Delta y^{\ell=0} = \Delta z^{\ell=0} = R/8$ and a level-1 discretization $\Delta x^{\ell=1} = \Delta y^{\ell=1} = \Delta z^{\ell=1} = R/16$.

System	Domain size ($L \times W \times H$)	D
System 1	$8R \times 4R \times 8R$	Breakup
System 2	$12R \times 4R \times 8R$	Breakup
System 3	$8R \times 4R \times 6R$	0.541
System 4	$8R \times 6R \times 6R$	0.466
System 5	$8R \times 8R \times 8R$	0.460
System 6	$8R \times 16R \times 16R$	0.460

Here we investigate the drop dynamics sensitivity to domain size around the critical Reynolds number $Re_{\mathrm{c}} = 0.75$. Specifically, we consider domain size sensitivity for the condition of $Re = 0.75$, $Ca = 0.3$, and $\lambda = \eta = 1$, which is a condition used in the comparison studies of the previous section. As shown in Table I, the drop breaks up for the condition of $Re = 0.75$ and $Ca = 0.3$ with a domain size of $L(8R) \times W(4R) \times H(8R)$. Results for domain size sensitivity for six domain systems, all of which use a level-1 grid size $\Delta x^{\ell=1} = \Delta y^{\ell=1} = \Delta z^{\ell=1} = R/16$, are tabulated in Table III. Note that the domain size used in the comparison study (Table I) corresponds to System 1.

The results in Table III suggest that drop deformation is promoted when we use a domain size with $W = 4R$. In contrast, the drop does not break up and becomes stable with a deformed shape if we set L large enough and $W \geq 6R$ and $H \geq 6R$. Since the value of D for the domain size $L(8R) \times W(6R) \times H(6R)$ differs by only 1.3% with the value for the domain size of $L(8R) \times W(16R) \times H(16R)$, in the results that follow we set the width to $W = 6R$ and the height to $H = 6R$ to minimize the number of computational grid nodes along those directions. To determine the critical Reynolds number Re_{c} (with $Ca = 0.3$), we consider a domain size of $L(24R) \times W(6R) \times H(6R)$, and we find that the drop reaches a stable state with deformation parameter $D = 0.549$ for $Re = 1.0$, while a value of $Re = 1.1$ leads to drop breakup.

2. Selecting the appropriate grid size

The grid size and adaptive meshing strategy that we adopt is chosen in order to answer the research question as to the conditions which determine whether a bubble in shear flow will break-up or not. In such a case, we must accurately capture the balance of forces with respect to the (non-local) force exerted from the wall driven flow acting against the interfacial surface tension force. The accuracy of the "Critical Reynolds Number" depends on the largest Taylor Deformation parameter D that is supported by the grid (see e.g. Figures 8 and 11). As we report here, we
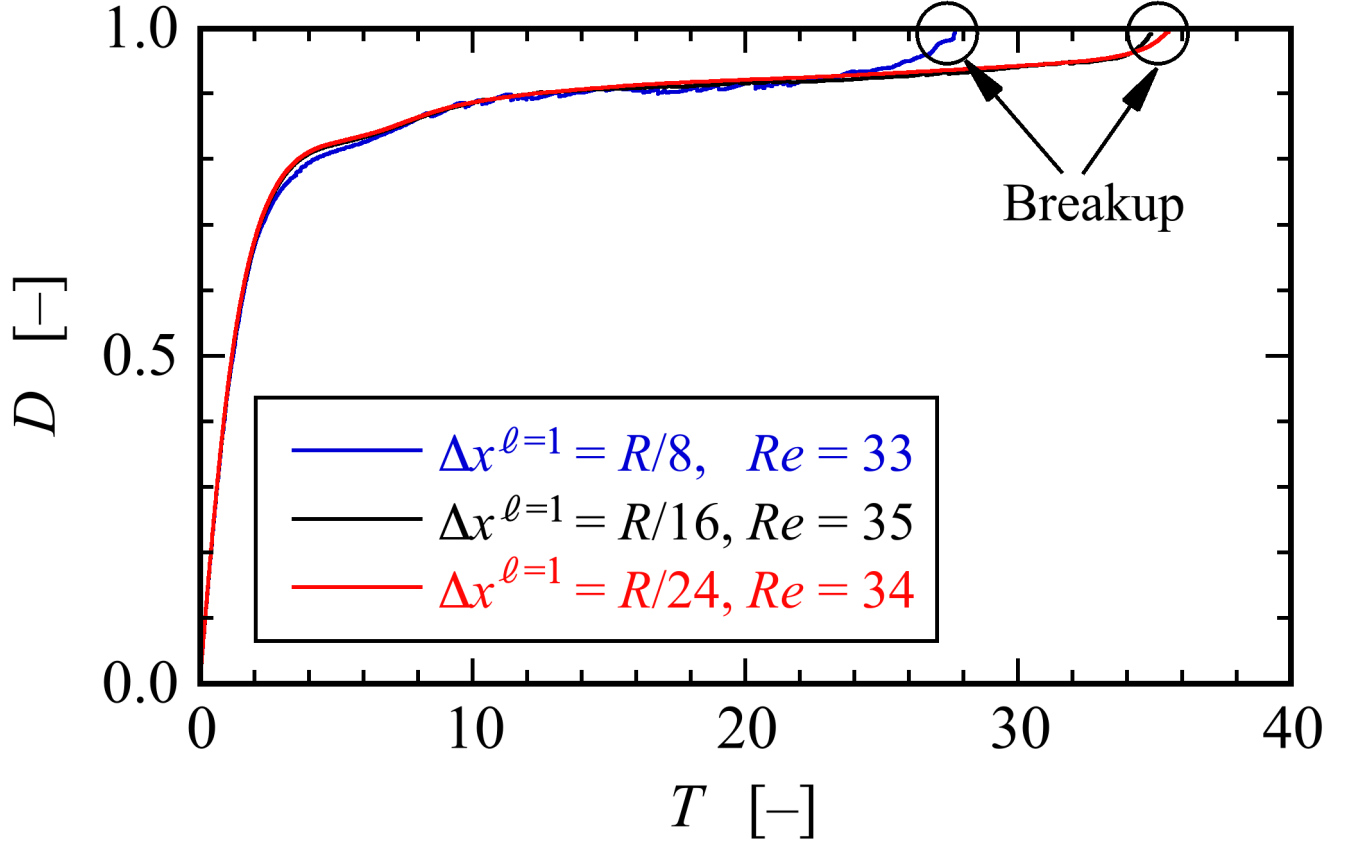
FIG. 3. Time evolution of the deformation parameter D versus dimensionless time $T = \Gamma t$ for a bubble, obtained with three grid systems at different resolutions. All three resolutions use a two-level AMR grid with an effective fine resolution grid size $\Delta x^{\ell=1} = \Delta y^{\ell=1} = \Delta z^{\ell=1}$. The evolution of D using the first system, where $\Delta x^{\ell=1} = R/8$, is shown in blue and it predicts that bubble breakup occurs at a Reynolds number $Re = 33$. The evolution of D using the second system, where $\Delta x^{\ell=1} = R/16$, is shown in black and it predicts that bubble breakup occurs at a Reynolds number $Re = 35$. Results with the third system, shown in red, use $\Delta x^{\ell=1} = R/24$, and they predict that breakup occurs at $Re = 34$. The capillary number corresponding to these results is $Ca = 1.0$. ($\lambda = 1.2 \times 10^{-3}$, $\eta < 1.0 \times 10^{-3}$)

have found that as long as the grid size is fine enough to support a Taylor Deformation parameter $D < 0.95$, then the transition region (i.e. "Critical Reynolds number") (see Figures 3 and 12) will be captured with a tolerance of three percent. The simulation time becomes impractical if we were to try to further improve the "critical Reynolds number" accuracy. A smaller tolerance would necessitate a larger supported Deformation parameter D which would in turn necessitate a higher aspect ratio computational domain, increased droplet surface area at break-up, increased number of time steps, and higher resolution for representing the drop/bubble at its thinnest point.

We make the distinction between our present research, and the research found in the work of Zang, Ni, and Magnaudet[47, 48] on predicting the conditions for bubble mergers. Even in the most extreme cases for mergers, the largest Deformation parameter never exceeds 0.4 in [47]. In summary, our gridding requirements necessitate grid points distributed relatively evenly throughout the computational domain when a bubble is stretched to a $D = 0.9$ Deformation, whereas in [47] the gridding strategy necessitates a more localized strategy.

The numerical results presented in this and the previous section used a finest-level grid size set to $\Delta x^{\ell=1} (= \Delta y^{\ell=1} = \Delta z^{\ell=1}) = R/16$. To verify the adequacy of this grid resolution, we present rid refinement results for a bubble breakup simulation with $Ca = 1.0$, which corresponds to the most deformable and stretchable bubble case considered in our numerical studies. We use three different grid systems, (i) $\Delta x^{\ell=1} = R/8$, (ii) $\Delta x^{\ell=1} = R/16$, and (iii) $\Delta x^{\ell=1} = R/24$, in order to determine Re_{c}. Figure 3 shows the time evolution of the deformation parameter D over time for the three grid systems; the x-axis is a dimensionless time defined by $T = \Gamma t$ and the y-axis is D. The results show that bubble breakup occurs at $Re_{\mathrm{c}} = 35$ for the grid system with $\Delta x^{\ell=1} = R/16$, while the finer computational grid with $\Delta x^{\ell=1} = R/24$ predicts a critical value of $Re_{\mathrm{c}} = 34$. For the $\Delta x^{\ell=1} = R/8$ results, it is clear that the $R/8$ resolution is too coarse in order to capture the proper break-up time, albeit the critical Reynolds' number, $Re_{\mathrm{c}} =$
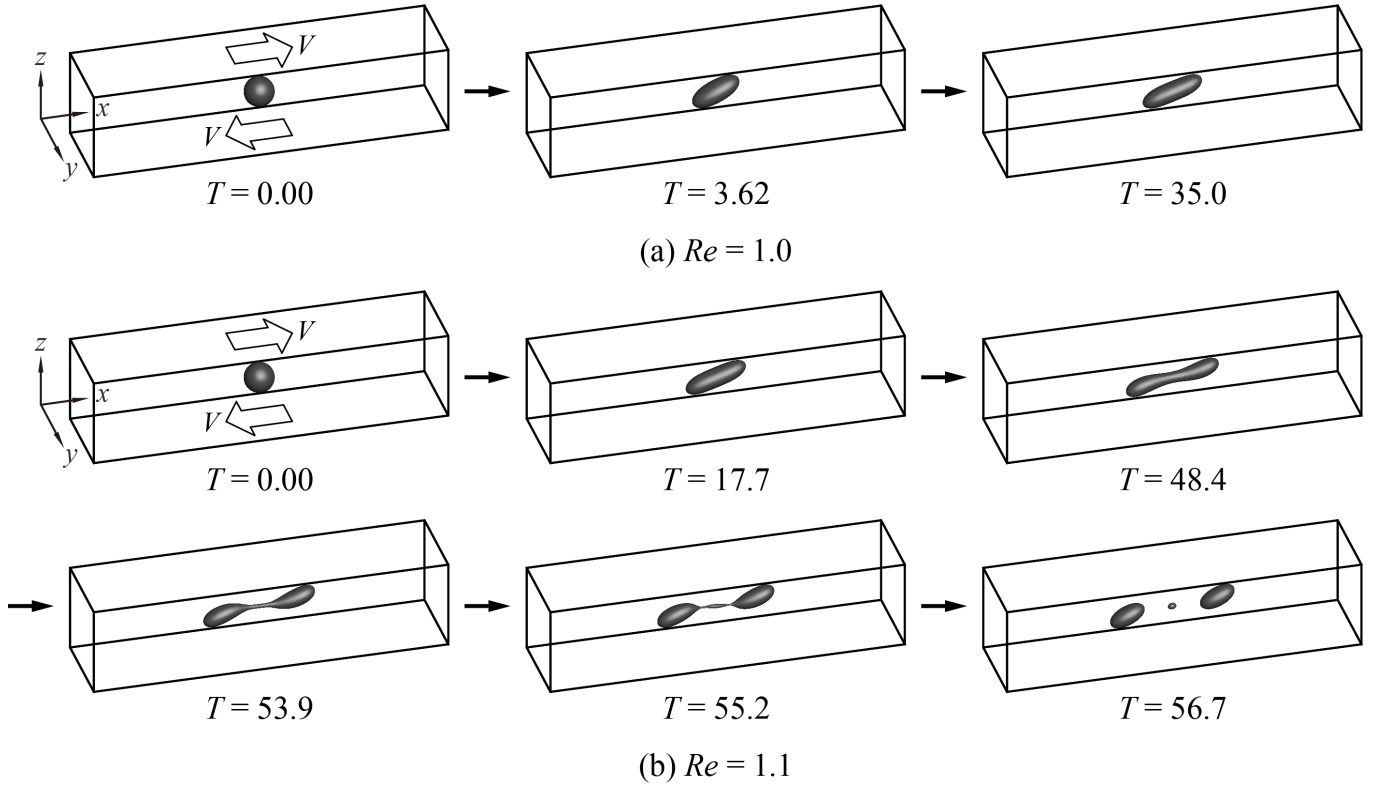
FIG. 4. Time evolution of drop deformation and breakup in shear flow at the condition of $Ca = 0.3$ with (a) $Re = 1.0$ and (b) $Re = 1.1$. The "drop" critical Reynolds number corresponding to $Ca = 0.3$ is $1.0 < Re_c < 1.1$. ($\lambda = \eta = 1.0$)

33, was still close to the finer grid resolution cases. Note that although the time evolution of D for the two finer resolution systems ($R/16$ and $R/24$) is consistent between the two, (the predicted critical Reynolds numbers differ by $\sim 3\%$), the computational time using the grid system with $\Delta x^{\ell=1} = R/24$ was more than 6 times longer than the one based on the coarser system with $\Delta x^{\ell=1} = R/16$. We remark that in our search for Re_c, we considered a wide range of values of Ca and we found it necessary to use a large L ($\sim 24R$) since for certain shear flows the bubble can stretch significantly without breaking up. Nevertheless, for the conditions presented in this section, the results indicate that our numerical approach, even with a finest-level resolution set to $\Delta x^{\ell=1} = R/16$, is capable of accurately reproducing bubble deformation and breakup without sacrificing any essential dynamical features.

IV. RESULTS AND DISCUSSION

A. Drop deformation and breakup

To illustrate the differences in deformation and breakup between a drop and a bubble around critical conditions, we first present numerical results for drop deformation. The time evolution of drop deformation and breakup in simple linear shear flow for two conditions is shown in Figure 4; the first case, shown in Figure 4(a), uses $Ca = 0.3$ and $Re = 1.0$, while the second case, depicted in Figure 4(b), uses $Ca = 0.3$ and $Re = 1.1$. Using a domain size of $L(24R) \times W(6R) \times H(6R)$, in the case with $Re = 1.0$, the drop gradually deforms and finally attains a stable deformed state with $D = 0.549$. Over the same domain, for the case with $Re = 1.1$, the "mother" drop elongates over time and the volume at the ends of the deforming drop expands; that is, both ends of the drop become bulb-shaped. As time progresses, particularly over the time interval $48.4 \le T \le 55.2$, a thread-bridge forms between the bulbous ends and the thread-bridge becomes thinner. Finally, at around the dimensionless time $T \sim 56.7$, the mother drop breaks up, forming two "daughter" drops through the pinch off; one satellite drop is also generated between the pinched off daughter drops.
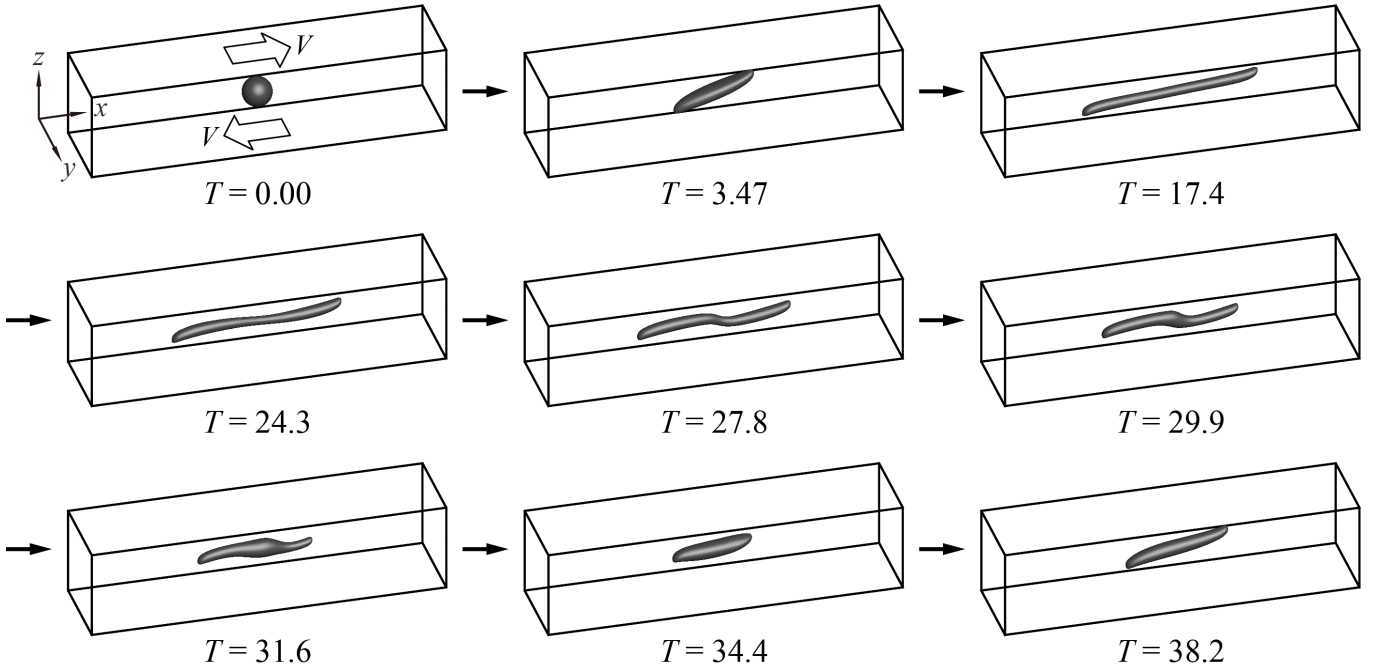
FIG. 5. Time evolution of bubble deformation in shear flow at the condition of $Ca = 0.3$ and $Re = 92$. The "bubble" critical Reynolds number corresponding to $Ca = 0.3$ is $92 < Re_c < 93$. In contrast to the drop deformation case, when Re is slightly below Re_c (See Figure 4 $Re = 1.0$ for the drop case), the bubble shape will not reach a steady shape, instead the bubble shape alternates between the shapes "slightly stretched" ($T = 3.47$), fully stretched and "doglegged" ($T = 27.8$) and "almost" back to the original "slightly stretched" case ($T = 34.4$). ($\lambda = 1.2 \times 10^{-3}$, $\eta < 1.0 \times 10^{-3}$)

B. Bubble deformation and breakup

Next we present numerical results that illustrate the conditions that lead to bubble deformation without breakup as well as conditions where the bubble deforms and ultimately breaks up. The time evolution of shear-induced bubble deformation without breakup at the condition of $Ca = 0.3$ and $Re = 92$ is depicted in Figure 5 and the bubble breakup process with flow condition of $Ca = 0.3$ and $Re = 93$ is illustrated in Figure 6. The results indicate that the critical Reynolds number is approximately $Re_c = 93$ (with $Ca = 0.3$). A comparison with the drop breakup dynamics presented in Section IV A and the corresponding processes for bubble deformation and breakup exhibit very distinct features. First, we note that a relatively large shear force magnitude is required for bubble breakup ($\lambda = 1.2 \times 10^{-3}$, $\eta < 1.0 \times 10^{-3}$) compared with the case of the drop ($\lambda = \eta = 1$). Then, for the same value of $Ca = 0.3$, the critical Reynolds number for the bubble is around 85 times larger than that for the drop. Focusing on the bubble dynamics with no-breakup (Figure 5), the results show that the bubble is largely elongated in the x-direction at the early stages ($T \leq 24.3$) of bubble deformation, but the bubble does not develop the bulb-like shape (large volume areas) at both ends present in the drop deformation process. It is also evident that the ends of the deforming bubble develop cusped shapes under the influence of the strong shear flow. A noteworthy feature for the non-breaking bubble is that it does not settle into a deformed stable state as in the case of drop deformation presented in Figure 4(a). After an initial elongation process, the bubble enters a shrinking phase ($T = 27.8$) where the doglegged shape formed at the center of the bubble returns to a smaller deformed shape ($T = 34.4$) that is similar to its earlier shape ($T = 3.47$). However, when we compare the early deformed bubble shape at $T = 3.47$ with the shape at $T = 34.4$, it is clear that the shapes are not identical. Following the shrinking phase, the bubble begins to stretch again ($T = 38.2$) and the bubble oscillates between its elongated shape and shortened geometry.

For the case of bubble breakup (Figure 6), we observe that the deformation process is almost the same as the no-breakup case until the doglegged shape is formed at $T \sim 27.4$. The bubble finally breaks during the time interval $27.7 \leq T \leq 29.5$. For a closer examination of the bubble breakup process, a detailed panel of cross-sectional slices in the xz-plane through the bubble shape center is presented in Figure 7. The images displayed in Figure 7, which are taken at shorter time intervals than those shown in Fig. 6, reveal that the bubble breaks up into two daughter bubbles due to the pinch off at the thread-bridge part of the doglegged shape during the shrinking process ($T = 28.5 \sim 28.8$). After breaking up, the two daughter bubbles migrate to the center: the left daughter bubble moves toward the right-
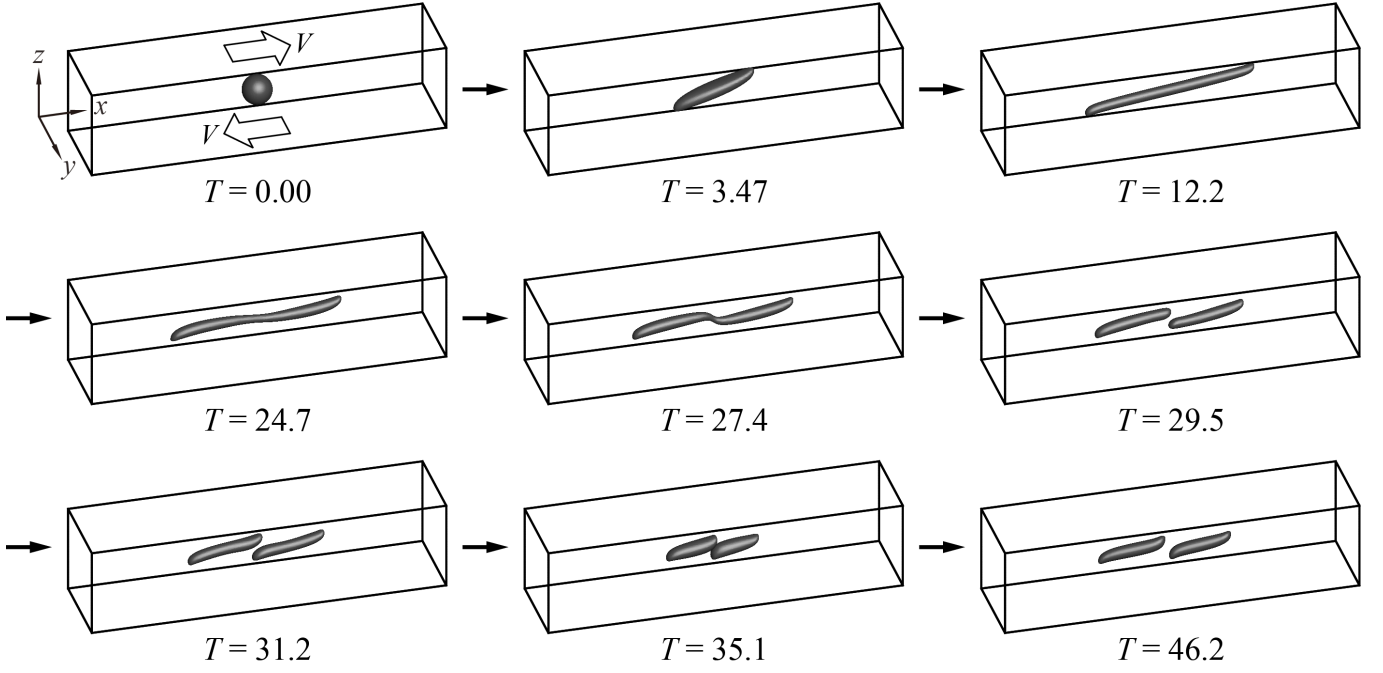
FIG. 6. Time evolution of bubble deformation in shear flow at the condition of $Ca = 0.3$ and $Re = 93$. The "bubble" critical Reynolds number corresponding to $Ca = 0.3$ is $92 < Re_c < 93$. ($\lambda = 1.2 \times 10^{-3}$, $\eta < 1.0 \times 10^{-3}$)
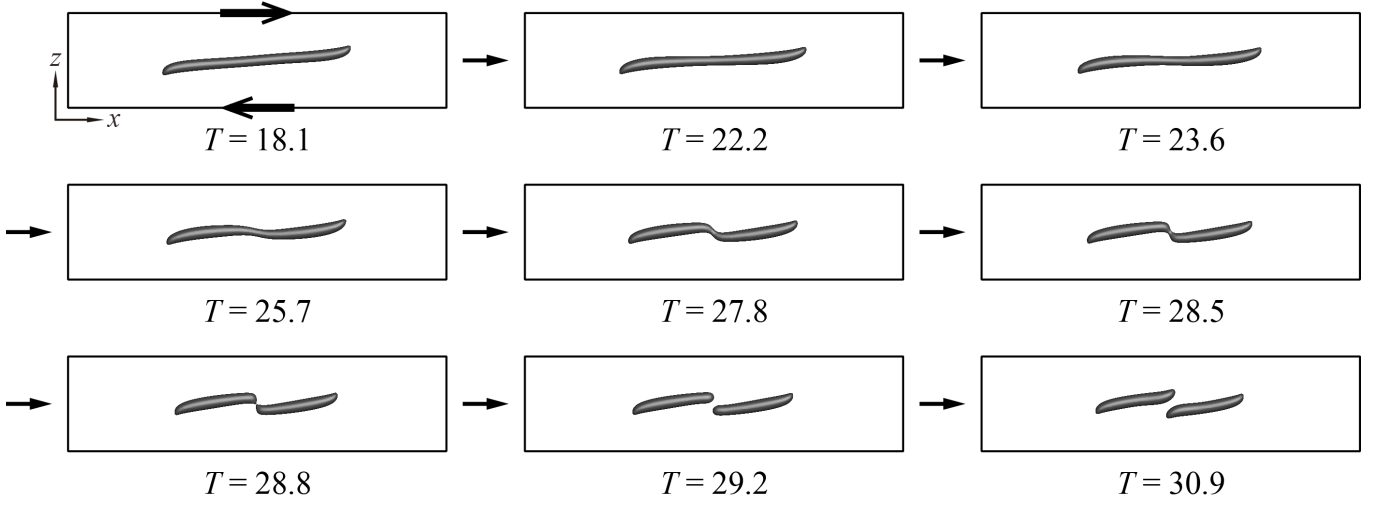

FIG. 7. Detail of bubble breakup process in shear flow at the condition of $Ca = 0.3$ and $Re = 93$. The "bubble" critical Reynolds number corresponding to $Ca = 0.3$ is $92 < Re_c < 93$. ($\lambda = 1.2 \times 10^{-3}$, $\eta < 1.0 \times 10^{-3}$)

side of the domain and the right daughter bubble moves to the left side (see results for $T = 29.5 \sim 35.1$ in Figure 6 and for $T = 28.8 \sim 30.9$ in Figure 7). The two daughter bubbles then momentarily congregate near the domain center ($T = 35.1$ in Figure 6), before they slowly start to separate: the left daughter bubble moves to the left and the right daughter bubble moves to the right ($T = 46.2$ in Figure 6). The results clearly demonstrate that the bubble breakup process is markedly different from the analogous drop breakup process.

C.   Shear stress acting on the bubble

In the previous section, the appearance of bubble deformation and breakup was discussed. It is expected that a large deformation and breakup of the bubble are closely related to the state of shear stress acting on the bubble.
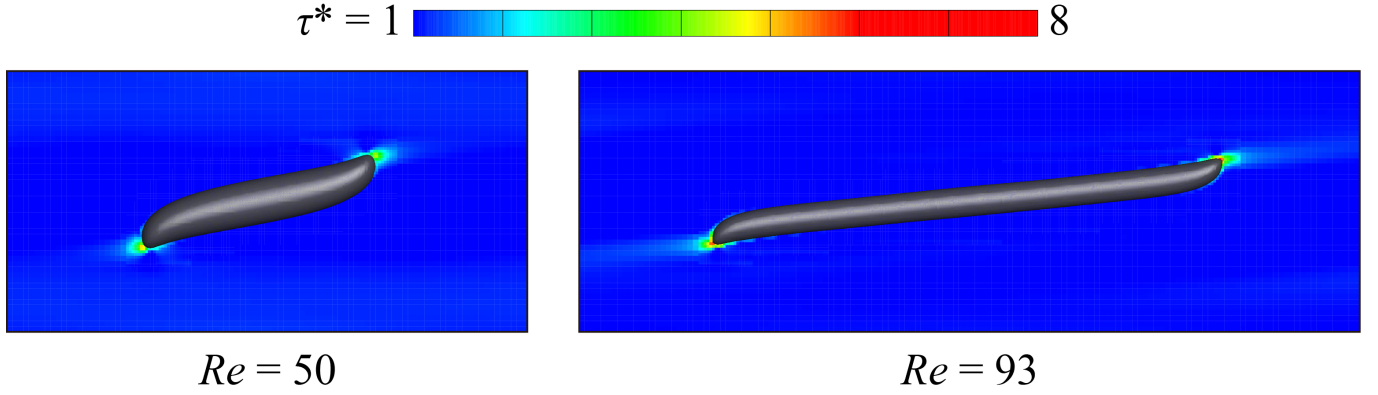
FIG. 8. Normalized shear stress τ^* around a bubble for two Reynolds numbers under the condition of $Ca = 0.3$. The left image shows the shear stress profile at $Re = 50$ and the right image at $Re = 93$.

Figure 8 shows the shear stress profile around a bubble for two Reynolds numbers under the condition of $Ca = 0.3$: Reynolds number equal to 50 and 93. The shear stress profile on the left corresponds to the case of $Re = 50$ and the right side shows the shear stress profile for the case of $Re = 93$. The normalized shear stress, $\tau^* = \tau/\tau_0$, is defined as a ratio of the local shear stress $\tau = \mu_m \sqrt{2\mathbf{D}:\mathbf{D}}$ and the apparent shear stress $\tau_0 = \mu_m \Gamma$. In this study, for a given Ca condition, the same value of τ_0 is used regardless of Re.

For the case of $Re = 50$, the bubble reaches a deformed stable state.

As observed in previous sections, when the value of Re is slightly below the critical Re condition, the bubble does not settle into a deformed stable state but instead alternates in an elongation and contraction process. In comparison to the $Re = 50$ case on the left, the right image in Fig. 8 ($Re = 93$) shows a higher shear stress profile near the bubble endpoints as it undergoes an elongation state in the process toward breakup. The value of the maximum shear stress for the case of $Re = 50$ is $\tau^* \approx 6$ and the maximum shear stress for the case of $Re = 93$ at the moment shown in Fig. 8 has the value of $\tau^* \approx 8$. The shear stress profile in Fig. 8 (color contour) is drawn in the range from $\tau^* = 1$ to $\tau^* = 8$, but, for emphasis, shear stress regions with $\tau^* \geqq 6$ are illustrated in red. As can be seen in the figure, the strongest shear stresses are concentrated on the ends of the bubble for both Re conditions. This indicates that the strong shear stresses acting on the ends of the bubble are responsible for much of the bubble stretching. It is important to note that the magnitude of the shear stress acting on the ends of the bubble for the case of $Re = 93$ is much larger than that for the case of $Re = 50$.

We also observe that the shear stress *inside* the bubble was very small relative to that of the matrix fluid due to very small density and viscosity of the bubble. Since the force of strong shear stresses acting on the ends of the bubble is difficult to transfer across the interface, as a consequence, a sufficiently large Re condition is required for large bubble deformations.

In summary, what we discover is that for the Reynolds number sufficiently below the critical value, a relatively quick unsteady elongation period gives way to a steady state (with no break up). On the otherhand for Reynolds number *close* to the critical Reynolds number, there is a prolonged, unsteady, elongation period, in which periodic motion is observed and the deformation parameter D is close to one. The "vacillating" behavior cannot last forever, ultimately (perhaps stochastically!), the bubble will either settle down or break. We assert that regardless of the outcome, this vacillating behaviour will always occur in close proximity to the critical Reynolds' number. In otherwords, regardless of the outcome, we claim, using the grid resolution of $R/16$, that one is assured of being within 3 percent of the critical Reynolds number (see Figure 3). In fact, we hypothesize that there will *always* be "vacillating" behavior if one is sufficiently close to the critical Reynolds number. i.e. given an almost infinite supply of computational resources, as one hones in closer and closer to the critical Reynolds number, a "tug of war" will be observed between the surface tension force trying to pull the bubble together versus the wall driven shear stress trying to pull the bubble apart.

D. Velocity field outside and inside the breaking bubble

In this section, we consider the fluid flow velocity field outside and inside the bubble during the shear-induced breakup process. Figure 9 shows the velocity fields outside and inside the bubble at cross-sectional slices in the xz-plane for a flow condition of $Ca = 0.3$ and $Re = 93$. Regions around the bubble where there is a higher density of velocity vectors correspond to the level-1 grid portion of the AMR structure. The simulation results show that the
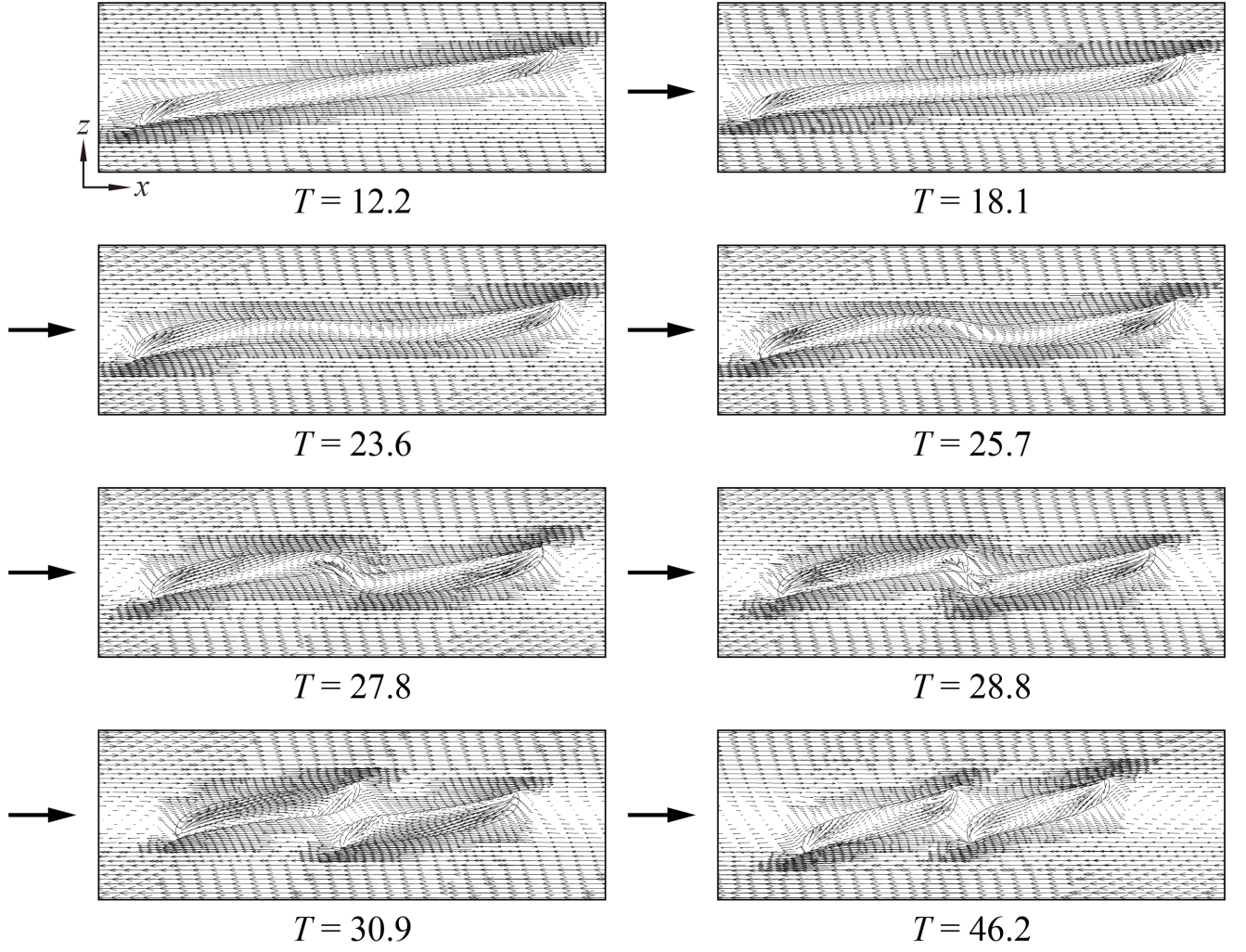
FIG. 9. Fluid velocity field outside and inside the breaking bubble in shear flow at the condition $Ca = 0.3$ and $Re = 93$. The "bubble" critical Reynolds number corresponding to $Ca = 0.3$ is $92 < Re_c < 93$. ($\lambda = 1.2 \times 10^{-3}$, $\eta < 1.0 \times 10^{-3}$)

velocity field inside the bubble is particularly distinct from the surrounding flow field in the exterior of the bubble. The cross-sections at $T = 12.2$ and $T = 18.1$, taken during the elongation phase, show how shear forces at the lower and upper halves of the bubble act along the bottom and top surfaces, respectively, to deform the interface. Near the left and right edges of the bubble, inward interior flows (that point toward the bubble center) begin to develop. Strong shearing forces in the exterior near the bottom-left-end and top-right-end of the bubble interact with the interior flow field through the boundary to create cusped shapes at the bottom-left and top-right ends of the bubble while the interface is laterally elongated in the x-direction. During the shrinking process, which occurs for $23.6 \leq T \leq 27.8$, inward flows within the bubble extend over a wider region and are no longer localized near the bubble edges. Then, we observe that circulating flows form at the thread-bridge part of the doglegged bubble shape over the time interval $[25.7, 27.8]$. During the breakup process ($T \sim 28.8$), higher-intensity inward flows are formed inside the bubble, near the pinch off region, that are naturally larger than the surrounding interior flows and which are inextricably associated with the bubble migration illustrated in Figs. 6 and 7. As time proceeds further ($T = 46.2$), distinct inward flows are formed inside the daughter bubbles; the bubbles then begin their migration toward the side walls. Considering the left daughter bubble, for example, we see that the mechanism responsible for this movement results from larger shear forces acting on the bottom-left end than those in the top-left end.
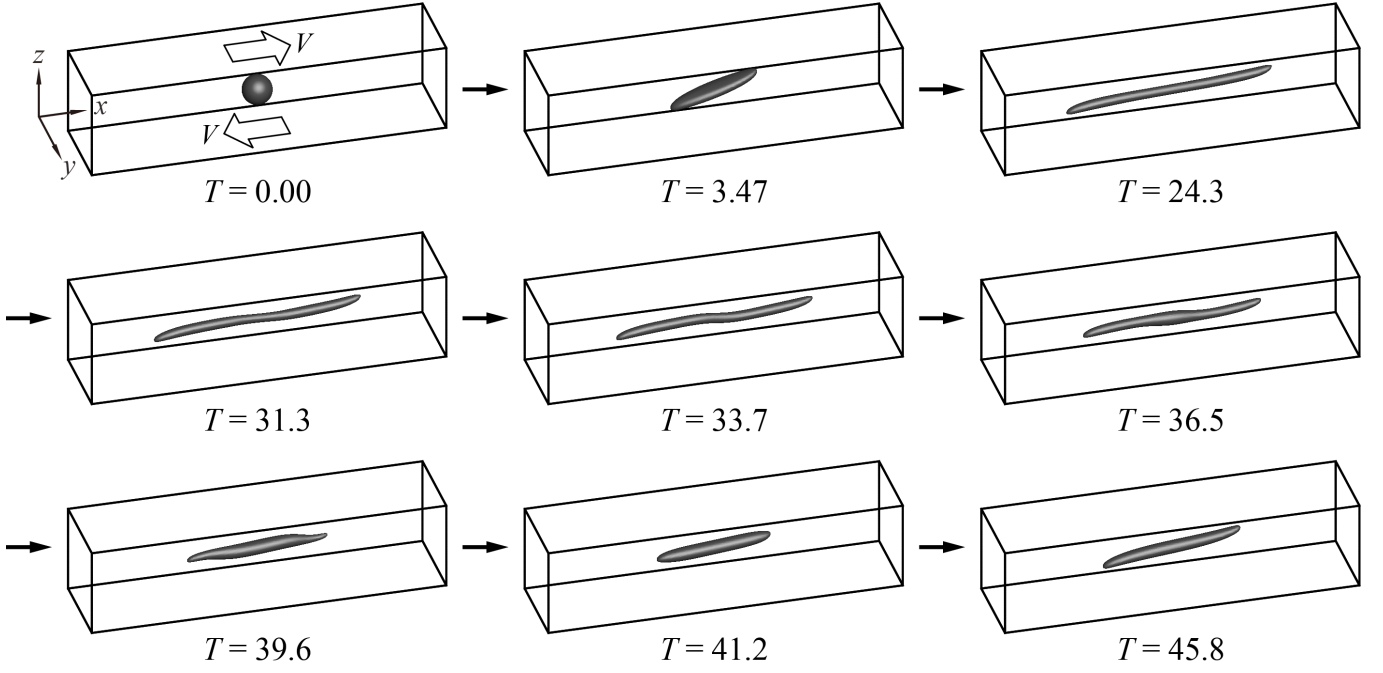
FIG. 10. Time evolution of bubble deformation in shear flow at the condition of $Ca = 0.8$ and $Re = 42$. The "bubble" critical Reynolds number corresponding to $Ca = 0.8$ is $42 < Re_c < 43$. ($\lambda = 1.2 \times 10^{-3}$, $\eta < 1.0 \times 10^{-3}$)
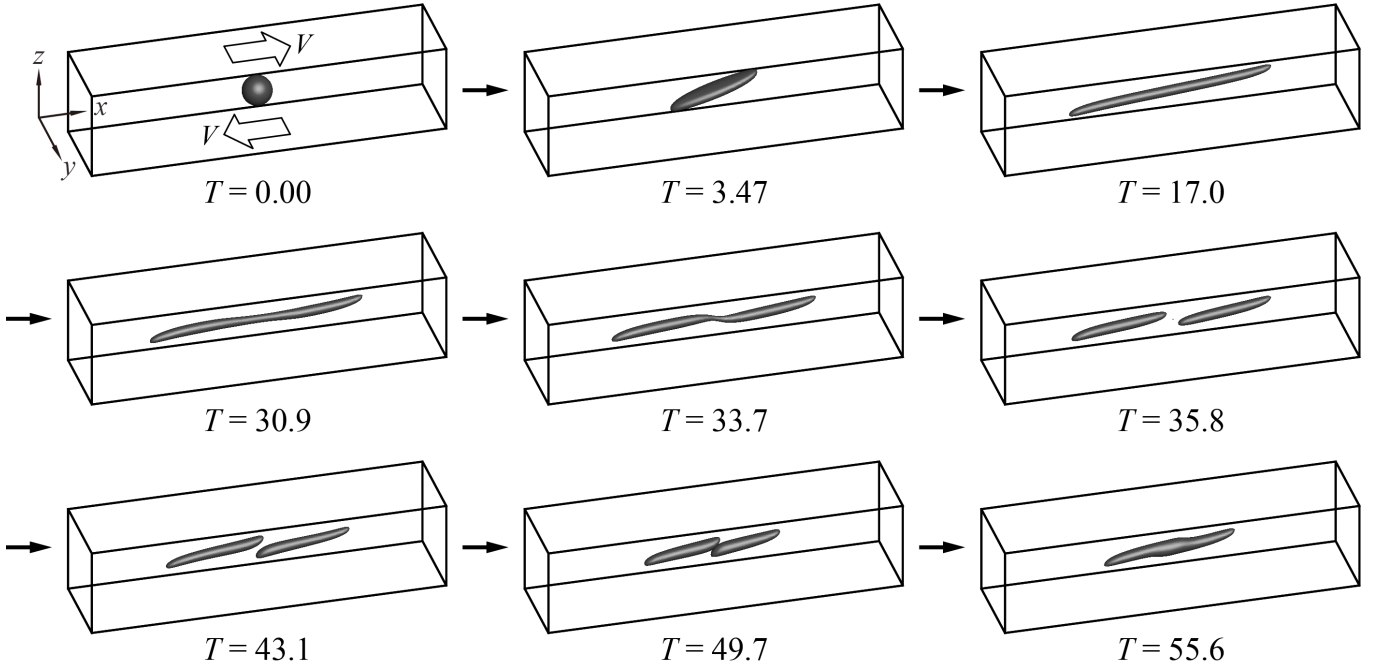

FIG. 11. Time evolution of bubble deformation in shear flow at the condition of $Ca = 0.8$ and $Re = 43$. The "bubble" critical Reynolds number corresponding to $Ca = 0.8$ is $42 < Re_c < 43$. ($\lambda = 1.2 \times 10^{-3}$, $\eta < 1.0 \times 10^{-3}$)

E.   Effect of surface tension on bubble deformation and breakup

In previous sections, we considered numerical simulations of bubble deformation and breakup with a Capillary number $Ca = 0.3$. Here, we examine similar bubble dynamics with $Ca = 0.8$ and we also investigate the effect of interfacial tension on bubble deformation and breakup. Using $Ca = 0.8$ for both cases, Figures 10 and 11 present the

time evolution of shear-induced bubble deformation and breakup with $Re = 42$ and $Re = 43$, respectively. We note that the bubble critical Reynolds number is around $Re_c \approx 43$, whereas $Re_c \approx 0$ for the corresponding case of the drop with $\lambda = \eta = 1$ (see e.g. [6]). Note that Re_c for $Ca = 0.8$ is smaller than that for the condition of $Ca = 0.3$ since the bubble at $Ca = 0.8$ is more elastic due to the weaker effect of surface tension in this case. The results shown in Figs. 10 and 11 indicate that the bubble deformation and breakup process for the condition of $Ca = 0.8$ is analogous to that for $Ca = 0.3$. For the case of bubble deformation without breakup (Fig. 10), the bubble initially assumes a long elongated shape along the x-direction at around $T = 24.3$. The bubble then enters a compression stage over the time interval $[31.3, 41.2]$ and subsequently starts to elongate again at $T = 45.8$. On the other hand, for the case of bubble breakup (Fig. 11), an initial elongation phase is followed by a doglegged shape formation at $T = 33.7$. After that, the bubble ruptures from the thread-bridge part of the doglegged shape and two daughter bubbles are produced ($T = 35.8$). The two daughter bubbles formed after breakup move to the central area ($T = 49.7$) as in the case of $Ca = 0.8$ and $Re = 93$, but the two bubbles eventually coalesce in a region approximately centered in the computational domain ($T = 55.6$). We note that in a real experimental setting, bubbles may coalesce after breaking up due to slight deviations of flow conditions and states. Although the process of bubble deformation and breakup for flow conditions with $Ca = 0.3$ and $Ca = 0.8$ are similar, a pronounced difference is that the bubble for $Ca = 0.8$ is more elongated and slender than that for $Ca = 0.3$ due to the smaller effect of surface tension for $Ca = 0.8$.

Table IV lists, for representative Ca values, the corresponding critical Reynolds number, Re_c, for shear-induced bubble breakup. The data in Table IV corresponds to $\lambda = 1.2 \times 10^{-3}$, $\eta < 1.0 \times 10^{-3}$, $0.3 < Ca < 1$, and the initial/boundary conditions are given by (1). The results in Table IV indicate that sufficiently large shear forces are required for bubble breakup even for large Capillary numbers. In Figure 12 we plot the smooth interpolant of the data given in Table IV and make the hypothesis that given a new data point, (Ca, Re), shear induced bubble break up will occur if the point (Ca, Re) is above the given critical curve, and the bubble will not break if the (Ca, Re) pair is below the critical curve. For comparison, a critical curve for the drop with $\lambda = \eta = 1$ is also indicated in Fig. 12. The inclusion of breakup and no-breakup critical curves, for both the drop and the bubble, will facilitate future identification of Re_c numbers—and thus a more complete general critical curve—for a wide range of high Ca numbers.

TABLE IV. Shear-induced bubble breakup for various flow conditions described in terms of column pairs of critical Reynolds numbers and corresponding Capillary numbers. ($\lambda = 1.2 \times 10^{-3}$, $\eta < 1.0 \times 10^{-3}$)

Capillary number Ca	0.3	0.5	0.8	1.0
Critical Reynolds number Re_c	93	67	43	35

V. CONCLUSIONS

The bubble deformation and breakup process in simple linear shear flow liquid was explored numerically using the CLSVOF computational method. In this study, the critical Reynolds number Re_c, at which bubble breakup first occurs, was determined for several flow conditions, and the differences between bubble deformation and breakup were compared with the well-known analogous process of drop deformation and breakup.

Numerical results revealed significant differences between bubble deformation and breakup and the corresponding drop dynamics. For case of bubble, it was discovered that much stronger shear flows are necessary to induce interface breakup compared with a drop immersed in a similar flow field. That is, a much larger Reynolds number flow is required in order to induce bubble breakup. The behavior of bubble breakup was very similar through the Ca number range considered in our computations: the bubble underwent a similar breakup mechanism in which rupture occurred at a thread-bridge part that followed a doglegged shape formation stage. In bubble deformation without breakup, near Re_c, the bubble did not maintain a stable deformed shape, in contrast to drop deformation near the critical Reynolds number. The bubble exhibited pronounced underdamped behavior: the bubble oscillated between elongating and shrinking motions for non-rupturing flow conditions.

We attribute the large differences in morphology for the bubble undergoing breakup, compared with the drop, to the density and viscosity ratio. The density and viscosity ratio remarkably impacts on bubble/drop deformation and breakup. The bubble deformation and breakup is subject to a synergistic coupling of the density and viscosity ratio,
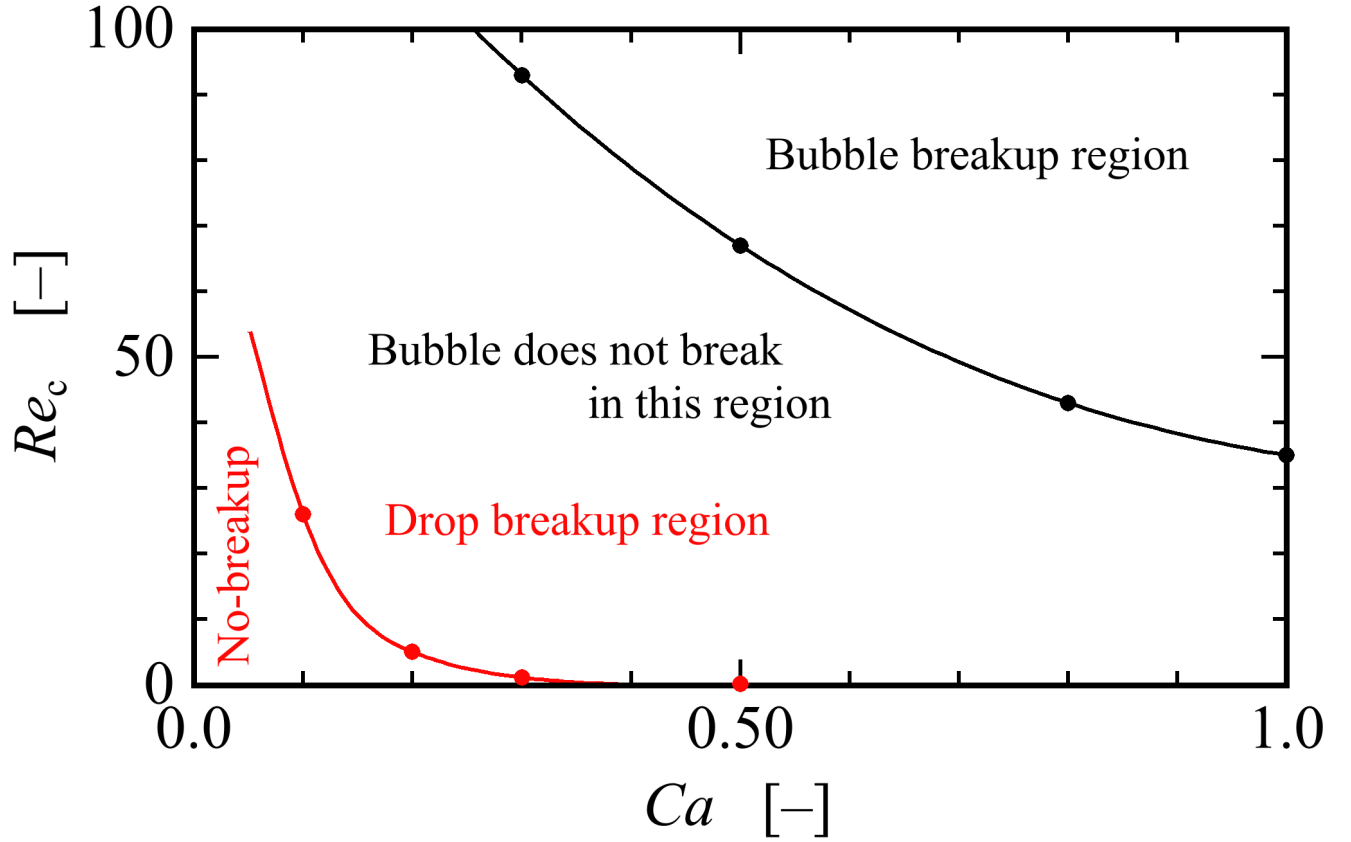
FIG. 12. A plot of the critical Reynolds number versus Capillary number for the data listed in Table IV. $\lambda = 1.2 \times 10^{-3}$, $\eta < 1.0 \times 10^{-3}$, $0.3 < Ca < 1$, and the initial/boundary conditions are given by (1). Given a new data point, (Ca, Re), one can reliably predict whether the given (Ca, Re) pair will result in shear induced bubble break-up or not. Note, for the "Drop delineation curve," $\lambda = \eta = 1$.

and whose effect will be examined separately in future work.

[1] G. I. Taylor, The viscosity of a fluid containing small drops of another fluid, Proceedings of the Royal Society of London A: Mathematical, Physical and Engineering Sciences **138**, 41 (1932).
[2] G. I. Taylor, The formation of emulsions in definable fields of flow, Proceedings of the Royal Society of London A: Mathematical, Physical and Engineering Sciences **146**, 501 (1934).
[3] J. M. Rallison, The deformation of small viscous drops and bubbles in shear flows, Annual Review of Fluid Mechanics **16**, 45 (1984), http://dx.doi.org/10.1146/annurev.fl.16.010184.000401.
[4] H. A. Stone, Dynamics of drop deformation and breakup in viscous fluids, Annual Review of Fluid Mechanics **26**, 65 (1994), http://dx.doi.org/10.1146/annurev.fl.26.010194.000433.
[5] C. Hirt and B. Nichols, Volume of fluid (vof) method for the dynamics of free boundaries, Journal of Computational Physics **39**, 201 (1981).
[6] J. Li, Y. Renardy, and M. Renardy, Numerical simulation of breakup of a viscous drop in simple shear flow through a volume-of-fluid method, Physics of Fluids **12**, 269 (2000).
[7] Y. Renardy and V. Cristini, Effect of inertia on drop breakup under shear, Physics of Fluids **13**, 7 (2001).
[8] Y. Y. Renardy and V. Cristini, Scalings for fragments produced from drop breakup in shear flow with inertia, Physics of Fluids **13**, 2161 (2001), https://doi.org/10.1063/1.1384469.
[9] Y. Renardy, V. Cristini, and J. Li, Drop fragment distributions under shear with inertia, International Journal of Multiphase Flow **28**, 1125 (2002).
[10] D. B. Khismatullin, Y. Renardy, and V. Cristini, Inertia-induced breakup of highly viscous drops subjected to simple shear, Physics of Fluids **15**, 1351 (2003).
[11] Y. Renardy, Numerical simulation of a drop undergoing large amplitude oscillatory shear, Rheologica acta **45**, 223 (2006).

[12] Y. Renardy, The effects of confinement and inertia on the production of droplets, Rheologica Acta **46**, 521 (2007).

[13] Y. Renardy, Effect of startup conditions on drop breakup under shear with inertia, International Journal of Multiphase Flow **34**, 1185 (2008).

[14] V. Cristini, S. Guido, A. Alfani, J. Bławzdziewicz, and M. Loewenberg, Drop breakup and fragment size distribution in shear flow, Journal of Rheology **47**, 1283 (2003).

[15] T. Inamuro, R. Tomita, and F. Ogino, Lattice boltzmann simulations of drop deformation and breakup in simple shear flows, International Journal of Modern Physics B **17**, 21 (2003).

[16] J. Zhang, M. J. Miksis, and S. G. Bankoff, Nonlinear dynamics of a two-dimensional viscous drop under shear flow, Physics of Fluids **18**, 072106 (2006).

[17] I. B. Bazhlekov, P. D. Anderson, and H. E. Meijer, Numerical investigation of the effect of insoluble surfactants on drop deformation and breakup in simple shear flow, Journal of Colloid and Interface Science **298**, 369 (2006).

[18] P. Janssen and P. Anderson, A boundary-integral model for drop deformation between two parallel plates with non-unit viscosity ratio drops, Journal of Computational Physics **227**, 8807 (2008).

[19] R. Croce, M. Griebel, and M. A. Schweitzer, Numerical simulation of bubble and droplet deformation by a level set approach with surface tension in three dimensions, International Journal for Numerical Methods in Fluids **62**, 963 (2010).

[20] A. Komrakova, O. Shardt, D. Eskin, and J. Derksen, Lattice boltzmann simulations of drop deformation and breakup in shear flow, International Journal of Multiphase Flow **59**, 24 (2014).

[21] A. Komrakova, O. Shardt, D. Eskin, and J. Derksen, Effects of dispersed phase viscosity on drop deformation and breakup in inertial shear flow, Chemical Engineering Science **126**, 150 (2015).

[22] N. Ioannou, H. Liu, and Y. Zhang, Droplet dynamics in confinement, Journal of Computational Science **17**, 463 (2016), discrete Simulation of Fluid Dynamics 2015.

[23] F. H. Hernandez and R. H. Rangel, Breakup of drops in simple shear flows with high-confinement geometry, Computers & Fluids **146**, 23 (2017).

[24] A. Amani, N. Balcázar, J. Castro, and A. Oliva, Numerical study of droplet deformation in shear flow using a conservative level-set method, Chemical Engineering Science **207**, 153 (2019).

[25] J. Zhang, S. Shu, X. Guan, and N. Yang, Regime mapping of multiple breakup of droplets in shear flow by phase-field lattice boltzmann simulation, Chemical Engineering Science **240**, 116673 (2021).

[26] V. Cristini, J. Bławzdziewicz, and M. Loewenberg, An adaptive mesh algorithm for evolving surfaces: simulations of drop breakup and coalescence, Journal of Computational Physics **168**, 445 (2001).

[27] P. J. A. Janssen and P. D. Anderson, Boundary-integral method for drop deformation between parallel plates, Physics of Fluids **19**, 043602 (2007).

[28] T. Inamuro, Lattice boltzmann methods for viscous fluid flows and for two-phase fluid flows, Fluid Dynamics Research **38**, 641 (2006).

[29] S. O. Unverdi and G. Tryggvason, A front-tracking method for viscous, incompressible, multi-fluid flows, Journal of Computational Physics **100**, 25 (1992).

[30] M. Sussman, P. Smereka, and S. Osher, A level set approach for computing solutions to incompressible two-phase flow, Journal of Computational Physics **114**, 146 (1994).

[31] E. Ervin and G. Tryggvason, The rise of bubbles in a vertical shear flow, Journal of Fluids Engineering **119(2)**, 443 (1997).

[32] D. Legendre and J. Magnaudet, The lift force on a spherical bubble in a viscous linear shear flow, Journal of Fluid Mechanics **368**, 81 (1998).

[33] Y. K. Wei, Y. Qian, and H. Xu, Lattice boltzmann simulations of single bubble deformation and breakup in a shear flow, The Journal of Computational Multiphase Flows **4**, 111 (2012), https://doi.org/10.1260/1757-482X.4.1.111.

[34] Z. Wang, D. Shi, and A. Zhang, Three-dimensional lattice boltzmann simulation of bubble behavior in a flap-induced shear flow, Computers & Fluids **123**, 44 (2015).

[35] P. Chu, J. Finch, G. Bournival, S. Ata, C. Hamlett, and R. J. Pugh, A review of bubble break-up, Advances in Colloid and Interface Science **270**, 108 (2019).

[36] N. Müller-Fischer, P. Tobler, M. Dressler, P. Fischer, and E. J. Windhab, Single bubble deformation and breakup in simple shear flow, Experiments in fluids **45**, 917 (2008).

[37] D. Bento, R. O. Rodrigues, V. Faustino, D. Pinho, C. S. Fernandes, A. I. Pereira, V. Garcia, J. M. Miranda, and R. Lima, Deformation of red blood cells, air bubbles, and droplets in microfluidic devices: Flow visualizations and measurements, Micromachines **9**, 10.3390/mi9040151 (2018).

[38] W. Drenckhan and A. Saint-Jalmes, The science of foaming, Advances in Colloid and Interface Science **222**, 228 (2015), reinhard Miller, Honorary Issue.

[39] M. Sussman and E. G. Puckett, A coupled level set and volume-of-fluid method for computing 3d and axisymmetric incompressible two-phase flows, Journal of Computational Physics **162**, 301 (2000).

[40] M. Sussman, K. Smith, M. Hussaini, M. Ohta, and R. Zhi-Wei, A sharp interface method for incompressible two-phase flows, Journal of Computational Physics **221**, 469 (2007).

[41] A. Rust and M. Manga, Bubble shapes and orientations in low re simple shear flow, Journal of Colloid and Interface Science **249**, 476 (2002).

[42] S. Tanguy, T. Ménard, and A. Berlemont, A level set method for vaporizing two-phase flows, Journal of Computational Physics **221**, 837 (2007).

[43] M. Kang, R. P. Fedkiw, and X.-D. Liu, A boundary condition capturing method for multiphase incompressible flow, Journal of scientific computing **15**, 323 (2000).

[44] M. Sussman, A second order coupled level set and volume-of-fluid method for computing growth and collapse of vapor

bubbles, Journal of Computational Physics **187**, 110 (2003).

[45] M. Sussman, A. S. Almgren, J. B. Bell, P. Colella, L. H. Howell, and M. L. Welcome, An adaptive level set approach for incompressible two-phase flows, Journal of Computational Physics **148**, 81 (1999).

[46] M. Ohta, D. Kikuchi, Y. Yoshida, and M. Sussman, Robust numerical analysis of the dynamic bubble formation process in a viscous liquid, International Journal of Multiphase Flow **37**, 1059 (2011).

[47] J. Zhang, M.-J. Ni, and J. Magnaudet, Three-dimensional dynamics of a pair of deformable bubbles rising initially in line. part 1. moderately inertial regimes, Journal of Fluid Mechanics **920**, A16 (2021).

[48] J. Zhang, M.-J. Ni, and J. Magnaudet, Three-dimensional dynamics of a pair of deformable bubbles rising initially in line. part 2. highly inertial regimes, Journal of Fluid Mechanics **943**, A10 (2022).